Bounding Surface Models of Sands: Pitfalls of Mapping Rules for Cyclic Loading

K. I. Andrianopoulos, A. G. Papadimitriou, G. D. Bouckovalas
Geotechnical Dept., School of Civil Engineering, National Technical University of Athens, Greece

Keywords: elastoplasticity, bounding surface, constitutive model, cyclic loading, sands

ABSTRACT: This paper studies how various mapping rules for bounding surface models affect the simulated sand response. A distinction is made between bounding surface models with a finite or a vanished elastic region. The goal of the paper is achieved by implementing various mapping rules in a very simple bounding surface model for sands. The paper shows that simple mapping rules that work fine for monotonic loading are inappropriate for cyclic loading, while other mapping rules that appear appropriate for cyclic loading may lead to erroneous results.

1 Introduction

Elastoplastic modeling of sand behavior has proven a difficult task in the literature, especially for cyclic loading. Lately, issues like the combined effect of confining pressure and void ratio on monotonic sand response have been successfully addressed by incorporating the state parameter ψ (Been and Jefferies, 1985) in constitutive equations, either explicitly (e.g. Wood et al, 1994) or implicitly (e.g. Jefferies, 1993). For cyclic loading in particular, seminal works are the bounding surface models of Wang et al (1990) and Manzari and Dafalias (1997). The former achieved successful cyclic loading simulations for large cyclic strains by appropriately incorporating the ever-current last shear reversal point in the mapping rule, while the latter achieved similarly accurate simulations for any confining pressure and void ratio by explicitly introducing the ψ parameter for sizing the bounding and dilatancy surfaces. More recently, Papadimitriou and Bouckovalas (2002) achieved quantitative accuracy for all cyclic shear strain levels, by introducing a Ramberg-Osgood type response at small cyclic shear strains and an appropriately evolving fabric tensor effect for shearing under large cyclic shear strains. Obviously the foregoing list is not all-inclusive, but presenting such a list is not the goal of this paper. What is of interest here is that bounding surface models have generally proven more successful in simulating cyclic loading of sands than any other constitutive model type. Nevertheless, the quality of simulations of a bounding surface model is strongly depended on its mapping rule, i.e. on how the current effective stress $\boldsymbol{\sigma}$ is mapped to an image stress $\boldsymbol{\sigma}^{b,i}$ on the bounding surface. This paper explores the effect of various mapping rules on the simulated response by implementing them in a very simple bounding surface model platform presented in segment 2. The adopted mapping rules are presented in segment 3, while segment 4 presents typical results, focusing on undrained loading that is of grave importance for cyclic loading of sands. Obviously the goal of this paper is not to condemn or glorify specific mapping rules. Rather, this paper attempts merely to raise issues of accuracy and stability for the various rules and on how their effects are hided or revealed by various loading paths. Note that in this paper boldface characters denote second-order tensors.

2 Constitutive Model Platform

The constitutive model platform used here is a generic bounding surface model that adopts various constitutive ingredients from the literature in a simplified manner. It is characterized by a vanished elastic region and a bounding surface that is an open wedge with apex at the origin of axes and centered along the mean effective stress p-axis (where $\sigma_1 = \sigma_2 = \sigma_3$). In other words, its bounding surface is a Drucker-Prager cone, which is totally defined by its shape on the π-plane of the deviatoric stress-ratio $\mathbf{r}(=\mathbf{s}/p)$ space, where $\mathbf{s} = \boldsymbol{\sigma} - p\mathbf{I}$ is the deviatoric stress tensor and $\mathbf{I}$ the identity tensor (see Figure 1). The model assumes that sand response is elastic for stress paths with constant values of $\mathbf{r}$ (e.g. K_o-consolidation), but fully elastoplastic for stress paths that induce a change in the value of $\mathbf{r}$ (e.g. cyclic shearing paths). This basic assumption simplifies constitutive equations, since plastic strain calculations are governed by changes in $\mathbf{r}$ alone, and on how the $\mathbf{r}$ point 'moves' with respect to the bounding surface on the π-plane of $\mathbf{r}$-space.

Describing the constitutive model platform requires first the presentation of the generic constitutive equations of incremental elastoplasticity. In this paper, superscripts 'e' and 'p' denote elastic and plastic parts in the elasto-plastic stress and strain deconvolution, while a superposed dot over stress or strain quantities denote their rate. Hence, the plastic strain rate and the loading index Λ are given by:

$$\dot{\boldsymbol{\varepsilon}}^{\mathbf{p}} = \langle \Lambda \rangle \mathbf{R} \qquad ; \qquad \Lambda = \frac{\mathbf{L} : \dot{\boldsymbol{\sigma}}}{K_p} \qquad (1)$$

where $\mathbf{R}$ is the plastic potential, $< >$ denote the Macauley brackets, where $<\Lambda> = \Lambda$ if $\Lambda > 0$ (loading) and $<\Lambda> = 0$ for $\Lambda \leq 0$ (unloading or neutral loading), $\mathbf{L}$ is the loading direction, K_p is the plastic modulus and the symbol $:$ between two tensors denotes their scalar double inner product. Similarly, by decoupling the volumetric and the shear strain rates, the elastic strain rate is given by:

$$\dot{\boldsymbol{\varepsilon}}^{\mathbf{e}} = \frac{\dot{\mathbf{s}}}{2G} + \frac{\dot{p}}{3K} \mathbf{I} \qquad (2)$$

where G and K are the elastic shear and bulk moduli. Giving specific forms in G, K, $\mathbf{L}$, $\mathbf{R}$ and K_p fully defines the constitutive model platform. Hence, for simplicity:

$$G = B p_a \left(\frac{p}{p_a} \right)^{1/2} \qquad ; \qquad K = \frac{2(1+v)}{3(1-2v)} G \qquad (3)$$

where p_a is the atmospheric pressure, while B and v are model constants.

$\mathbf{L}$ and $\mathbf{R}$ are usually defined as the gradients to the yield and plastic potential surface, respectively, but in this constitutive model platform with a vanished elastic region, these are defined as:

$$\mathbf{L} = \mathbf{n} - \frac{\mathbf{n} : \mathbf{r}}{3} \mathbf{I} \qquad ; \qquad \mathbf{R} = \mathbf{n} + \frac{D}{3} \mathbf{I} \qquad (4)$$

where D is the (scalar) dilatancy coefficient and $\mathbf{n}$ is a unit deviatoric stress-ratio tensor ($\mathbf{n}:\mathbf{n}=1$, trace[$\mathbf{n}$]=0) that lies on the π-plane of the $\mathbf{r}$-space (see Figure 1).

What remain to be defined are the forms of the plastic modulus K_p and the dilatancy coefficient D. There are practically infinite ways of defining these two quantities. What is being used here is a simplified form of what a family of bounding models with a ψ-dependence of the model surfaces has proposed, like the models of Manzari & Dafalias (1997), Gajo and Wood (1999), Li & Dafalias (2000), Papadimitriou and Bouckovalas (2002), Dafalias et al (2004). Namely, besides the bounding surface, the model has also two more inter-related cone-shaped surfaces, a critical state surface and a dilatancy surface (see Figure 1). Specifically, if one defines M as the deviatoric stress-ratio value at critical state for any deviatoric loading direction $\mathbf{n}$ (and respective Lode angle θ) the corresponding M^b and M^d at the bounding and dilatancy surfaces are given by:

$$M^b = M\exp(-n^b \psi) \qquad ; \qquad M^d = M\exp(+n^d \psi) \qquad (5)$$

where n^b and n^d are model constants, and $\psi = e - e_{cs}$, where e is the current void ratio and e_{cs} is the e value on the critical state line for the current p value. Hence, this definition of ψ requires an explicit definition of the critical state line in the $e - p$ space, for which there are multiple proposals in

the literature in terms of 2 or 3 model constants.

The values of M^b and M^d from Equation (5) are then used for the definition of the image points $\mathbf{r}^{b,i}$ and $\mathbf{r}^{d,i}$ on the two surfaces, according to (see also Figure 1):

$$\mathbf{r}^{b,i} = (2/3)^{1/2} M^b \mathbf{n} \qquad ; \qquad \mathbf{r}^{d,i} = (2/3)^{1/2} M^d \mathbf{n} \qquad (6)$$

Given these image points, one may define the respective 'distances' d^b and d^d as:

$$d^b = \left(\mathbf{r}^{b,i} - \mathbf{r}\right) : \mathbf{n} \qquad ; \qquad d^d = \left(\mathbf{r}^{d,i} - \mathbf{r}\right) : \mathbf{n} \qquad (7)$$

Having defined the model surfaces and their related 'distances', one may now define the remaining two model variables, the plastic modulus K_p and the dilatancy coefficient D, as:

$$K_p = Cp \frac{d^b}{\left\langle d^b_{ref} - d^b \right\rangle} = Chpd^b \qquad ; \qquad D = Ad^d \qquad (8)$$

where A and C are model constants, and h is a scaling function related to 'distance' d^b and a reference 'distance' ($d^b_{ref} > 0$) in terms of the bounding surface size ($d^b_{ref} = 2(2/3)^{1/2} M^b$). Note that d^b and d^d may also take negative values, leading to the simulation of strain softening and dilatant response, respectively. Finally, observe that only when both $\psi = 0$ and $d^b = d^d = 0$ are realized, the model predicts critical state failure (zero volumetric and infinite shear strain at constant stress $\boldsymbol{\sigma}$).
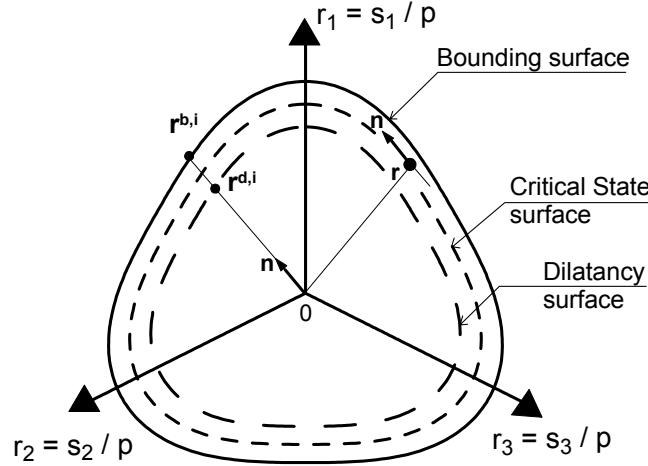
Figure 1. Model surfaces and image points

3 Mapping Rules

As can be deduced from the foregoing equations, the definition of the deviatoric loading direction $\mathbf{n}$ is of cardinal importance for the operation of the model, since it governs the plastic strain calculations in many respects. This segment explores the effects of defining $\mathbf{n}$ in various manners with emphasis on cyclic loading. If the constitutive model had a non-zero elastic region within its bounding surface, say in the form of a kinematically hardening cone (see Figure 2a, where both surfaces are shown circular for simplicity), then tensor $\mathbf{n}$ could be defined either along the component of the gradient to the yield surface on the π-plane (e.g. Gajo and Wood 1999), or along the direction of ($\mathbf{r} - \boldsymbol{\alpha}$), where $\boldsymbol{\alpha}$ is the deviatoric back stress-ratio tensor introducing the kinematic hardening of the yield surface (e.g. Manzari and Dafalias 1997, Papadimitriou and Bouckovalas 2002, Dafalias et al 2004). Either choice has proven successful for both monotonic and cyclic loading. On top of this, having a yield surface in the formulation adds stability, in the sense that small perturbations in the loading sequence (potentially of numerical origin) do not affect the results significantly, since the stress point perturbations remain mainly within the elastic region producing merely small elastic strains. On the other hand, having a yield surface in the formulation requires

addressing issues like the stress point crossing of the yield surface, the drift correction aiming at enforcing the consistency condition and the required sub-stepping in the integration scheme that increase significantly the computational effort. This increased computational effort requirement may prove very cumbersome in cases of boundary value problems with cyclic loading at hand (e.g. seismic excitation), and almost dictate the use of bounding surface model schemes with a vanished elastic region, which are numerically more efficient. Nevertheless, a version of the constitutive model with a small circular yield surface is also used here for comparison purposes. This version of the model defines **n** as follows:

$$\mathbf{n} = \frac{\mathbf{r} - \boldsymbol{\alpha}}{\left| \mathbf{r} - \boldsymbol{\alpha} \right|} \tag{9}$$

where $|\ |$ denote the norm of a tensor, while the kinematic hardening rule that is consistent with the K_p value of Equation (8) is given by:

$$\dot{\boldsymbol{\alpha}} = \langle \Lambda \rangle h \left(\mathbf{r}^{b,i} - \mathbf{r} \right) \tag{10}$$

The form of Equation (9) adds to the stability of the model, in the sense that if the applied loading changes direction, the deviatoric loading direction **n** remains as is, and only after some integration steps it re-adjusts appropriately, via Equation (10). Experience has shown that especially for cyclic loading this version of the model requires a yield surface of very small size, say radius $m = M/100$. Practically speaking, this version of the model with a yield surface is very reminiscent of the works of Manzari & Dafalias (1997) and Papadimitriou & Bouckovalas (2002). If the elastic region has diminished to the current stress point, then the definition of **n** requires an *ad hoc* assumption. For the purpose of this work, three (3) discretely different mapping rules have been used and compared parametrically with each other, as well as with the reference case of the model with a yield surface (denoted as *Rule_0* in the figures).

3.1 Mapping rule 1

Figure 2b presents mapping rule 1 in a schematic manner. Observe that the image point $\mathbf{r}^{b,i}$ is found from the projection of the current stress-ratio **r** along the direction of the elastic predictor of the deviatoric stress-ratio rate $\dot{\mathbf{r}}^e$ and that the deviatoric loading direction **n** (initiating from the apex) is along the $\mathbf{r}^{b,i}$. This mapping rule offers computational efficiency, but has the obvious disadvantage that a perturbation in the $\dot{\mathbf{r}}^e$ will affect the results, since it leads to a perturbation in the direction of **n** of a smaller amount. Nevertheless, this mapping rule (denoted as *Rule_1* in the figures) is more stable than its slight variation having the **n** being along the $\dot{\mathbf{r}}^e$ itself, since then a perturbation of the latter leads to a perturbation of the former tensor of an equal amount.

3.2 Mapping rule 2

Figure 2c presents mapping rule 2 in a schematic manner. Observe that the image point $\mathbf{r}^{b,i}$ is along either **r** or –**r**, depending on whether shearing is continued or reversed, respectively. In other words, this mapping rule (denoted as *Rule_2* in the figures) uses the apex as the projection center for $\mathbf{r}^{b,i}$. The criterion of shear reversal also requires definition. In this paper, shear reversal is set to occur when $\mathbf{n} : \dot{\mathbf{r}}^e < 0$. This mapping rule offers computational efficiency and also the benefit of stability, since only a large perturbation in $\dot{\mathbf{r}}^e$ may lead to shear reversal and thus to instability in the results. Actually, this mapping rule may prove too insensitive to the applied $\dot{\mathbf{r}}^e$, since $\mathbf{r}^{b,i}$ (and **n**) is linked to **r** for any $\dot{\mathbf{r}}^e$ pointing at an angle smaller than $\pm 90^o$ with respect to **r**.
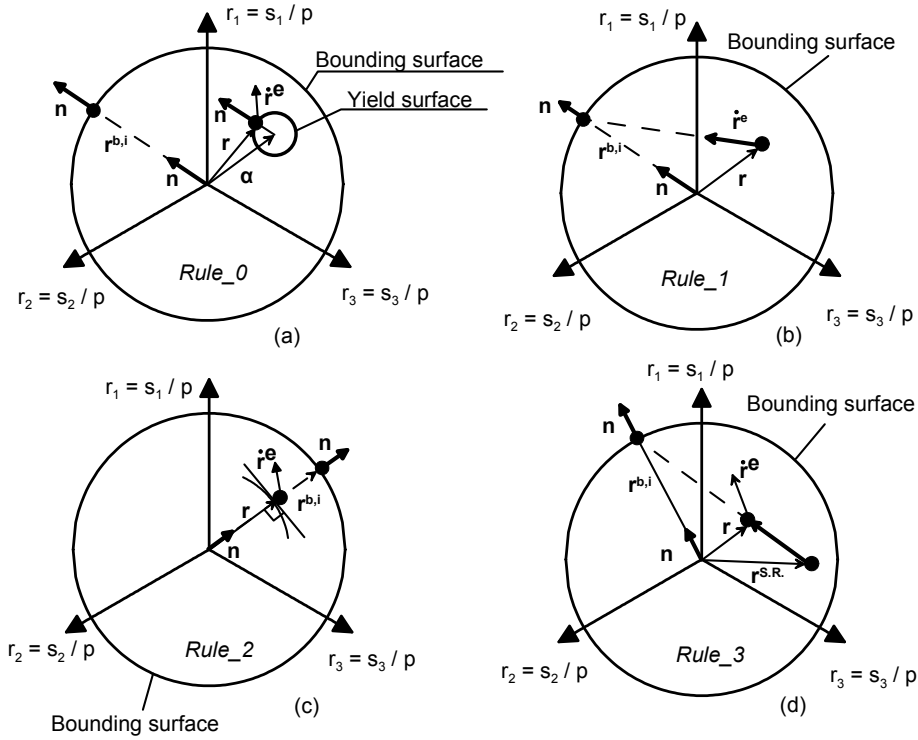
Figure 2. Mapping rules

3.3 Mapping rule 3

Figure 2d presents mapping rule 3 in a schematic manner. Observe that the image point $\mathbf{r}^{b,i}$ is found from the projection along the $(\mathbf{r} - \mathbf{r}^{SR})$ direction, where $\mathbf{r}^{SR}$ is the point of the last shear reversal that is used as a projection center for $\mathbf{r}^{b,i}$. The criterion of shear reversal used in this mapping rule (denoted as *Rule_3* in the figures) is same with that in *Rule_2*, namely shear reversal occurs when $\mathbf{n} : \dot{\mathbf{r}}^{e} < 0$. Nevertheless, this criterion puts importance on the recent shear history $(\mathbf{r} - \mathbf{r}^{SR})$, rather than the current $\mathbf{r}$ for both the definition of the image point $\mathbf{r}^{b,i}$. This makes *Rule_3* potentially more accurate, since $\mathbf{r}^{b,i}$ is the point where the $\mathbf{r}$ is heading rather than a projection of $\mathbf{r}$ itself. Overall, mapping *Rule_3* offers both computational efficiency and stability and has the potential for increased accuracy. Nevertheless, if a perturbation in $\dot{\mathbf{r}}^{e}$ leads to the definition of a new $\mathbf{r}^{SR}$ then the potential for accuracy may be lost. In conclusion, note that this mapping rule is very reminiscent of that used by Wang et al (1990).

4 Typical Results

In order to study how the three (3) mapping rules affect the response in various cases of shearing, parametric runs were performed using the constitutive model platform and the three (3) different mapping rules (*Rule_1*, *Rule_2*, *Rule_3*). In all cases, the version of the model with a small circular elastic region was also used for comparison purposes (*Rule_0*). All runs initiated from p = 100kPa, e = 0.86 (corresponding to ψ = -0.02) and used the same model constants (see Table 1) to enable one-to-one comparison. The calibration of the constants of the model platform is beyond the scope

of this paper, but follows the lines of the respective constants in the models of Manzari & Dafalias (1997) and Papadimitriou & Bouckovalas (2002). Finally, note that the model platform can easily incorporate strength anisotropy by making the M a function of the **n**-defined Lode angle θ. Nevertheless, in order to focus on the differences from the various mapping rules and not be influenced by side-effects from different M values, the M was considered equal to $M = 1.25$, and hence the Critical State, the Bounding and the Dilatancy surfaces are concentric circles on the π-plane of the **r**-space.

Table 1. Model Constants

Elasticity	Critical State	Plastic Modulus	Dilatancy
$B = 150$	$M = 1.25$	$C = 1000$	$A = 0.2$
$v = 1/3$		$n^b = 1.0$	$n^d = 1.0$

Figure 3 compares the response of the four (4) model versions for a monotonic undrained simple shear test starting from a $K_o = 1$ condition. The comparison is performed in terms of the effective stress path $p - q$, where $q = (3/2\ \mathbf{s{:}s})^{1/2}$, the second invariant of the deviatoric stress tensor. More specifically, Figures 3a, 3b and 3c compare the reference response of the model version with an elastic region (*Rule_0*) to the response from the model with the three mapping rules (*Rule_1*, *Rule_2*, *Rule_3*), respectively. Observe that all versions of the model predict exactly the same response. This is due to the fact that this path is radial in the π-plane of the **r**-space, namely it originates from the apex and extends outwards along a radius of the circular model surfaces. In other words, all versions of the model predict tensor **n** to be constant throughout shearing along the same radius, i.e. because the **n** is along $\mathbf{\dot{r}^e}$ and **r**. The same results would appear from a triaxial shearing path, because then again there is no principal stress rotation during shear. Specifically, in a triaxial compression test the major principal stress σ_1 is constantly vertical, in triaxial extension the σ_1 is constantly horizontal, while in this simple shear test it is constantly at 45° from vertical.

Figure 4 compares the response of the four (4) model versions for a monotonic undrained simple shear test starting from a $K_o = 0.4$ condition, in the format of Figure 3. Observe that the various mapping rules produce different results, and this because there is some principal stress rotation during shear (σ_1 initiates vertical and slowly rotates towards 45°). Of the three mapping rules, it is *Rule_3* that is closer to *Rule_0* because it defines $\mathbf{r^{SR}}$ at the beginning of the test and the $(\mathbf{r} - \mathbf{r^{SR}})$ gives an **n** direction very near the direction of $(\mathbf{r} - \boldsymbol{\alpha})$. On the other hand, it is *Rule_2* that is further away from *Rule_0*, since the **r** rotates much faster than the direction of $(\mathbf{r} - \boldsymbol{\alpha})$. Finally, *Rule_1* shows a response quite similar to *Rule_3*.

Figure 5 compares the response of the four (4) model versions for a cyclic undrained simple shear test starting from a $K_o = 0.4$ condition, in the same known three-plot format. The test is characterized by a constant cyclic shear stress ratio of $\tau_c = \pm 40$kPa. Observe that here the various mapping rules produce extremely different results and this is due to the extreme principal stress rotation during shear (σ_1 starts off vertical and rotates on either side of the vertical direction during each cycle). None of the three mapping rules succeeds in duplicating the results of the *Rule_0* model. Practically speaking, it is again *Rule_2* that produces the most different results (observe the much larger number of cycles). *Rule_1* and *Rule_3* produce very similar results, which are quite close to the reference results. Their similarity stems from the fact that at each load reversal the $\mathbf{\dot{r}^e}$ changes direction significantly, and so does the $(\mathbf{r} - \mathbf{r^{SR}})$ due to the activation of the shear reversal criterion at each half cycle.

Figure 6 compares the response of the four (4) model versions for an undrained simple shear test sequence starting from a $K_o = 0.4$ condition, in the same known three-plot format. The difference here is that the test sequence is not characterized by a constant τ_c. Rather it is a more or less random shearing test sequence, as one that could be observed in boundary value problems.

Namely, the sequence is a simple shear test including reversals of the applied shear strain, which is characterized by non-zero normal strains in the vertical and horizontal direction only between points 1 and 2. Nevertheless, the undrained condition is maintained throughout the test. This change in shearing conditions aims at simulating a loading perturbation in actual boundary value problems. Observe that *Rule_2* deviates from the very start from the rest, similarly to what was observed in Figures 4 and 5. On the other hand, *Rule_1* and especially *Rule_3* follow quite closely the reference results. Figure 6 implies that the imposed perturbation activated the shear reversal criterion used in *Rule_2*, and did have a significant effect on the results. This shows that mapping rules using a shear reversal criterion may provide stability with regard to small perturbation in $\dot{\mathbf{r}}^e$, but if this perturbation is large enough to activate their shear reversal criterion they may actually provide results, which are less accurate.

Overall, the use of $\dot{\mathbf{r}}^e$ in all studied mapping rules may be considered as less accurate compared to the actual elasto-plastic $\dot{\mathbf{r}}$. Nevertheless, in boundary value problems the latter is not known in the beginning of each integration step and only the former is readily available. Hence the use of $\dot{\mathbf{r}}$ practically requires solving each integration step iteratively, which beats the purpose of numerical efficiency. Furthermore, in cases where the model may predict strain softening (as the model in segment 2), a condition of $\mathbf{n} : \dot{\mathbf{r}} < 0$ could hold during continued shearing. In such a case, the use of the $\dot{\mathbf{r}}$ in the studied mapping rules would lead to erroneous results.

5 Conclusions

This paper compares the response of three (3) different mapping rules that could be potentially used for bounding surface models with a vanished elastic region simulating the cyclic loading of sands. The comparison is made against a reference version of the model with a small but non-zero elastic region. The basic conclusions from this study are the following:

- Before adopting any kind of mapping rule, this should be very carefully studied in various cases of shearing that include extreme principal stress rotation and small or large perturbations in the shearing sequence.
- Mapping rules including shear reversal criteria may provide some stability with regard to small perturbation in the shear reversal, but can produce unpredictable results if their criteria are activated.
- Defining the deviatoric loading direction $\mathbf{n}$ as the direction of the image point $\mathbf{r}^{b,i}$ induces stability to a mapping rule, even if this rule uses the numerically efficient $\dot{\mathbf{r}}^e$ which by default is sensitive to numerical perturbations.

6 References

Been K., Jefferies M.G. 1985. A state parameter for sands, *Geotechnique*, **35**(1), 99-112

Dafalias Y.F, Papadimitriou A.G., Li X.S. 2004. Sand plasticity model accounting for inherent fabric anisotropy, *Journal of Engineering Mechanics*, **130**(11), 1319-1333

Gajo A., Wood D.M. 1999. A kinematically hardening constitutive model for sands: the multiaxial formulation, *International Journal for Numerical and Analytical Methods in Geomechanics*, **23**(9), 925-965.

Jefferies M.G. 1993. Nor-Sand: a simple critical state model for sand, *Geotechnique*, **43**(1), 91-103.

Li X.S., Dafalias Y.F. 2000. Dilatancy for cohesionless soils, *Geotechnique*, **50**(4), 449-460

Manzari M.T., Dafalias Y.F. 1997. A critical state two-surface plasticity models for sands, *Geotechnique*, **47**(2), 255-272.

Papadimitriou A.G, Bouckovalas G.D. 2002. Plasticity model for sand under small and large cyclic strains: a multiaxial formulation, *Soil Dynamics and Earthquake Engineering*, **22**(3), 191-204.

Wang Z.L., Dafalias Y.F., Shen C.K. 1990. Bounding surface hypoplasticity model for sand, *Journal of Engineering Mechanics*, **116**(5), 983-1001

Wood D.M., Belkheir K., Liu D.F. 1994 Strain softening and state parameter for sand modelling, *Geotechnique*, **44**(2), 335-339
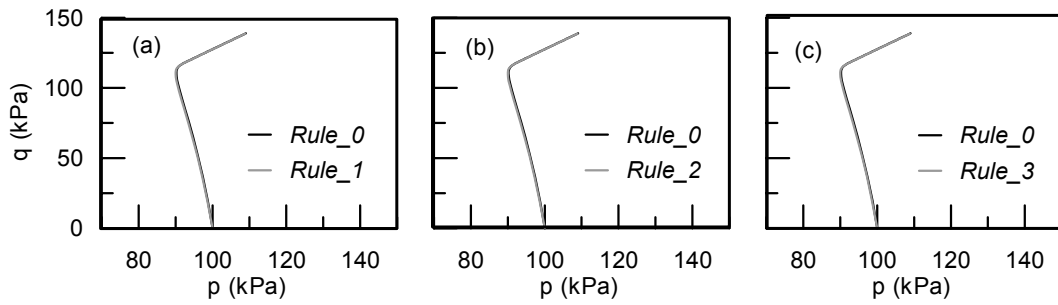
Figure 3. Effect of mapping rule on monotonic undrained simple shear (K_o=1.0)
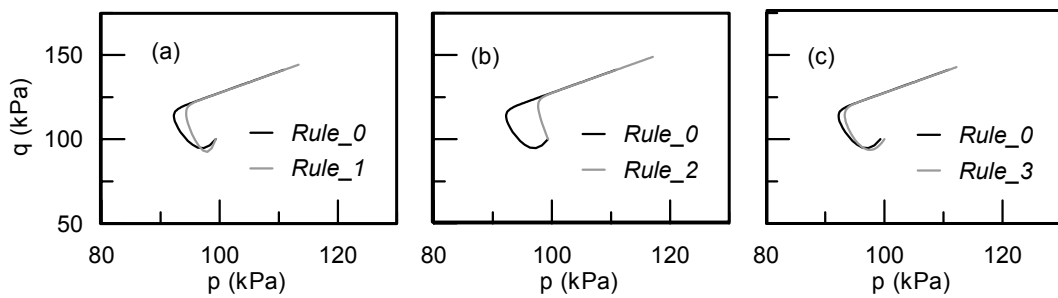
Figure 4. Effect of mapping rule on monotonic undrained simple shear (K_o=0.4)
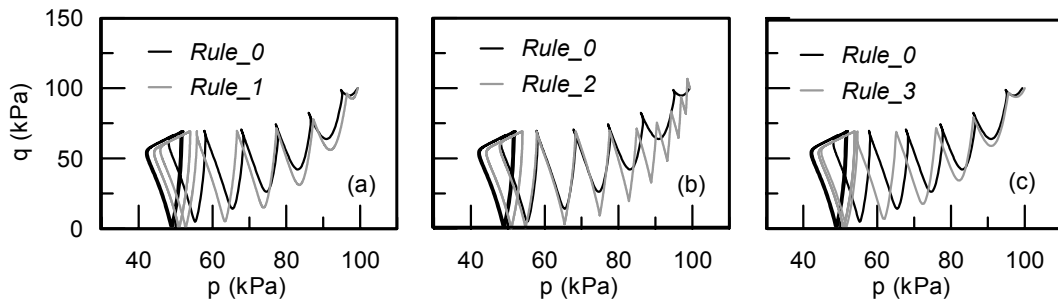
Figure 5. Effect of mapping rule on cyclic undrained simple shear (K_o=0.4)
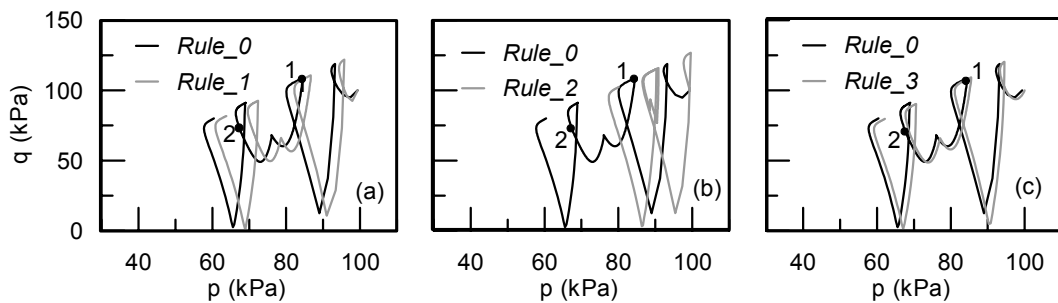
Figure 6. Effect of mapping rule on undrained simple shear test with numerical perturbations